Journal of
Applied
Crystallography

ISSN 1600-5767

Received 4 July 2013
Accepted 13 December 2013

Larmor neutron diffraction with one precession arm

M. T. Rekveldt,* J. Plomp and A. A. van Well

Department of Radiation Science and Technology, Faculty of Applied Sciences, Delft University of Technology, 2629JB Delft, The Netherlands. Correspondence e-mail: m.t.rekveldt@tudelft.nl

A new variant of Larmor neutron diffraction, applying only a single precession arm in the initial beam, is proposed. The single arm, together with the polarizer and analyser and possible rotators, are mounted in front of the sample. The great advantage with respect to the case with another precession arm in the reflected beam is that magnetic samples can now be investigated, because depolarization and the Larmor phase change of the beam polarization in the sample after the analyser is no longer of importance for diffraction analysis. The application has lower resolution than the double-arm precession geometry, but is still better than conventional diffraction instruments. The differences will be discussed.

1. Introduction

In Larmor diffraction, introduced as Larmor precession in high-resolution neutron diffraction in 1999 (Rekveldt & Kraan, 1999; Rekveldt *et al.*, 2001), the wavelength of the diffracted neutrons is determined by the precession angle in a field region of known dimensions and known field strength. The inclinations of the front and end faces of the precession region are chosen such that, after Bragg reflection of the neutron beam, the spread in precession angles due to the spread in wavelengths is greatly reduced, which means that the precession can be followed to very large precession angles. The precession angle that can be followed from a reflection on a specific lattice plane distance d is just the inverse of the resolution $\Delta d/d$ of that lattice spacing. In the original method, a double-arm precession geometry (DAG) is used, which means that the incident and diffracted beams both pass a precession device, as sketched in Fig. 1. In doing so, as explained below in more detail, the Larmor precession of a polarized neutron beam encodes both the wavelength and the incident neutron direction in such a way as to cancel the angular and wavelength dependence of the Larmor precession of the polarization of the diffracted neutrons. In this way the measured Larmor precession, which can be measured to very high values, directly yields the lattice spacing with extremely high precision ($\Delta d/d \simeq 10^{-6}$).

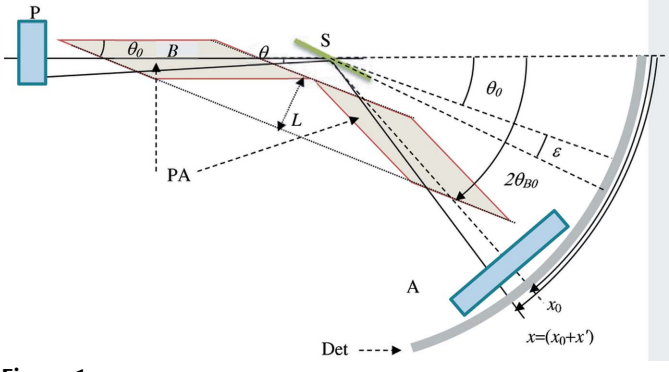

Figure 1
A sketch of the DAG. P and A are, respectively, the polarizer and analyser producing and analysing the polarization component perpendicular to the precession field B. The precession regions PA have faces inclined by θ_0 to the main axis and approximately parallel to the diffraction plane of the sample S, which makes an angle ε with θ_0.

The method has been applied successfully in the determination of lattice-spacing variations in Al and Si wafers (Rekveldt *et al.*, 2002), the determination of the absolute lattice spacing of Si powders and the study of the superalloy Inconel (Repper *et al.*, 2010), the study of very small lattice-constant variations in MnSi at low temperatures (Pfleiderer *et al.*, 2007), the study of the distribution of lattice constants and the antiferromagnetic moment in high-purity URu_2Si_2 (Niklowitz *et al.*, 2010), the investigation of the temperature dependence and distribution of lattice constants in $CePt_3Si$ (Ritz *et al.*, 2010; Sokolov *et al.*, 2011), and most recently the investigation of the link between structural and magnetic ordering in the $BaM_2(XO_4)_2$ family (M = Co, Ni; X = As, P) (Martin *et al.*, 2012) and of the magnetic ordering in metallic $Ba(Fe_{1-x}Mn_x)_2As_2$ (Innosov, 2013).

With somewhat less accuracy in lattice-spacing determination, Larmor diffraction can also be used in a much simpler setup that is discussed in this article. We will describe and discuss a single-arm variant (single-arm precession geometry, SAG), which has different properties but which is simpler to use and also has important advantages in diffraction studies of magnetized samples.

2. Instrument description

Although the DAG was historically first, from an instrumental point of view we prefer to describe here the SAG first and compare its properties with those of the DAG.

The precession arm consists of a parallelogram-shaped precession area with induction B perpendicular to that area and an inclination angle θ_0 of the front and end faces of the parallelogram with the main beam direction, and a diffracting sample with diffraction planes making a well defined angle ε

with the inclined faces of the precession area, as sketched in Fig. 2. To enable precession around B, the polarization vector created by the polarizer P in general has to be rotated first over $\pi/2$ by a rotator to a direction perpendicular to B in the precession region and then rotated back before the analyser A by a second rotator. For simplicity in describing these elements, the polarizer, analyser and rotators have been drawn as two units, P and A.

Consider a neutron with wavelength λ, entering a single- or polycrystalline sample at an angle θ with respect to the main axis, that reflects to an angular position x on the detector. When diffraction takes place from a crystal plane with lattice spacing d and an orientation $\theta_0 + \varepsilon$ (where $\varepsilon = \varepsilon_c + \varepsilon_v$, with ε_c a constant and ε_v the variable part, varying within $\Delta\varepsilon$), then the following parameters are of relevance for the measured polarization at x:

$$\begin{aligned} &x = x_0 + x' = 2\theta_B - \theta = 2(\theta_0 + \varepsilon_c + \varepsilon_v) + \theta, \\ &x_0 = 2\theta_{B0} \equiv 2(\theta_0 + \varepsilon_c), \\ &\text{thus } x' = \theta + 2\varepsilon_v. \end{aligned} \tag{1}$$

The angle θ represents the divergence of the incident beam, which we assume to be Gaussian with a width $\Delta\theta$. In the case of a single crystal, the variable part ε_v is simply the mosaic spread, and in a polycrystalline material it is the average deviation around the constant ε_c. The variable ε_v is determined by both the incident angle θ and the detection angle x'. The latter has an uncertainty Δx determined by the detector uncertainty and the finite size of the sample.

The polarization of the diffracted beam can be derived from the cosine of the precession angle averaged over θ and λ in the SAG

$$P = \left\langle \cos \varphi_s(\theta, \varepsilon, d, B) \right\rangle_{av}, \tag{2}$$

with

$$\begin{aligned} \varphi_s(\theta, \varepsilon, d, B) &= c\lambda(\theta, \varepsilon) B \frac{L}{\sin(\theta_0 + \theta)} \\ &\equiv 2cBLd \frac{\sin(\theta_0 + \theta + \varepsilon)}{\sin(\theta_0 + \theta)} \\ &= 2cBLd\left[\cos\varepsilon + \sin\varepsilon \cot(\theta_0 + \theta)\right]. \end{aligned} \tag{3}$$

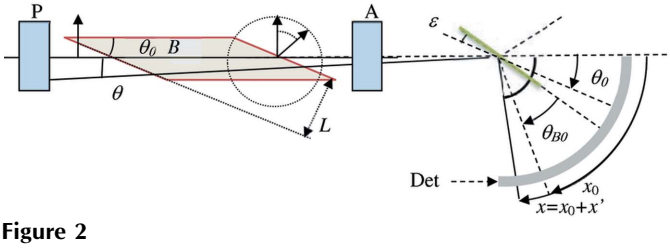

Figure 2
A sketch of the SAG. P and A are, respectively, the polarizer and analyser setting and analysing the polarization component (in the plane of the figure) perpendicular to the precession field B (perpendicular to the plane of the figure). The precession region has faces inclined by θ_0 to the main axis and a distance L between the faces. Intensity is measured on the detector (Det) at an angle x. The angle ε is the deviation angle between the diffracting plane and the inclination angle θ_0.

$c = \gamma h/m = 4.6368 \times 10^{14}\ \mathrm{T^{-1}\ m^{-2}}$, where h is the Planck constant, γ the gyromagnetic ratio and m the mass of a neutron. The precession angle $\varphi_s(\theta, \varepsilon, d, B)$ for some lattice spacing d and magnetic field B is no longer dependent on λ but only on θ and ε.

We first discuss the situation for a point-like detector with $\Delta x = 0$. Then it appears that $x' = 2\varepsilon_v + \theta$ must be constant and ε_v and θ are necessarily coupled variables. We can split the precession angle $\varphi_s(\theta, \varepsilon, d, B)$ into a constant part, $\varphi_{sc}(\varepsilon_c, x', d, B)$, and a variable part, $\varphi_{sv}(\varepsilon_v, \varepsilon_c, d, B)$. The former determines the oscillation frequency in P as a function of B, and the latter expresses the damping

$$\varphi_{sc}(\varepsilon_c, x', d, B) = 2cBLd\left(\cos\varepsilon_c + \sin\varepsilon_c \cot\theta_0 - \frac{x' \sin\varepsilon_c}{\sin^2\theta_0}\right), \tag{4}$$

$$\begin{aligned} &\varphi_{sv}(\varepsilon_v, \varepsilon_c, d, B) \\ &= 2cBLd\left[\varepsilon_v\left(-\sin\varepsilon_c + \cos\varepsilon_c \cot\theta_0 + \frac{2\sin\varepsilon_c}{\sin^2\theta_0}\right)\right], \end{aligned} \tag{5}$$

where we have used the first-order expansion of $\cot(\theta_0 + \theta) = \cot\theta_0 - \theta/\sin^2\theta_0$ for small θ. The variable part φ_{sv} can be made zero at a value of $\varepsilon_c = \varepsilon_{c0}$ given by

$$\tan\varepsilon_{c0} = \frac{\cos\theta_0 \sin\theta_0}{\sin^2\theta_0 - 2} \quad \text{or} \quad 2\tan\left(\frac{x_0}{2}\right) = \tan\theta_0. \tag{6}$$

However, the constant part $\varphi_{sc}(\varphi_c, x', d, B)$ now varies linearly in x'.

To compare these results with the case of the DAG, consider the sketch of the DAG in Fig. 1. We find here for the precession angle the sum of the precessions through two regions:

$$\begin{aligned} \varphi_d(\theta, \varepsilon, d, B) &= c\lambda(\theta, \varepsilon) B\left[\frac{L}{\sin(\theta_0 + \theta)} + \frac{L}{\sin(\theta_0 + \theta + 2\varepsilon)}\right] \\ &= 2cBLd\left[\frac{\sin(\theta_0 + \theta + \varepsilon)}{\sin(\theta_0 + \theta)} + \frac{\sin(\theta_0 + \theta + \varepsilon)}{\sin(\theta_0 + \theta + 2\varepsilon)}\right] \\ &= 2cBLd\big\{2\cos\varepsilon \\ &\quad + \sin\varepsilon\left[\cot(\theta_0 + \theta) - \cot(\theta_0 + \theta + 2\varepsilon)\right]\big\}. \end{aligned} \tag{7}$$

We now also split $\varphi_d(\theta, \varepsilon, d, B)$ into a constant part, $\varphi_{dc}(\varepsilon_c, x', d, B)$, and a variable part, $\varphi_{dv}(\varepsilon_v, \varepsilon_c, d, B)$, again using $2\varepsilon_v - x' = -\theta$, to yield

$$\begin{aligned} &\varphi_{dc}(\varepsilon_c, x', d, B) \\ &= 2cBLd\left\{2\cos\varepsilon_c + \sin\varepsilon_c\left[\cot\theta_0 - \cot(\theta_0 + 2\varepsilon_c)\right]\right. \\ &\quad \left. - x' \sin\varepsilon_c\left[\frac{1}{\sin^2\theta_0} - \frac{1}{\sin^2(\theta_0 + 2\varepsilon_c)}\right]\right\}, \end{aligned} \tag{8}$$

$$\begin{aligned} \varphi_{dv}(\varepsilon_v, \varepsilon_c, d, B) &= 2cBLd\left\{-2\varepsilon_v \sin\varepsilon_c\right. \\ &\left. + \varepsilon_v \cos\varepsilon_c\left[\cot\theta_0 - \cot(\theta_0 + 2\varepsilon_c)\right] + \sin\varepsilon_c\left(\frac{2\varepsilon_v}{\sin^2\theta_0}\right)\right\}, \end{aligned} \tag{9}$$

and here it appears that the variable part can be made zero at $\varepsilon_c = 0$, while at this value the constant $\varphi_{dc}(\varepsilon_c, x', d, B)$ also does not change with varying x'.

The ratio $\varphi_{dv}(\varepsilon_v, \varepsilon_c, d, B)$:$\varphi_{dc}(\varepsilon_c, x', d, B)$ for the SAG and DAG determines the damping of the measured polarization as a function of B. This ratio equals the achievable resolution $\Delta d/d$ of the setups. Fig. 3 shows the results for the SAG and DAG at $x' = 0$ and $\theta_0 = \pi/4$. The figure shows that, outside the points ε_{c0} where $\varphi_{(s,d)v}(\varepsilon_v, \varepsilon_c, d, B)$ is minimal, the resolution is roughly proportional to the variable part $|\varepsilon_v|$ with a proportionality factor about 0.01 times the deviation of ε_c from ε_{c0}.

The offset angle ε_{c0}, where precession damping is minimal, is dependent on the inclination angle θ_0, as found from equation (6). This dependence is shown in Fig. 4, where the Bragg angle $\theta_{B0} = \theta_0 + \varepsilon_{c0}$, with minimal damping, is plotted as a function of the inclination angle θ_0, together with its values when the Bragg reflection is out of the drawing plane (see Fig. 2) at the two angles given in the figure. The offset angle ε_{c0} can be chosen as required for an experiment.

It appears that the focusing condition derived in the scattering plane is present over an angular range greater than 5° out of the plane. This angle should not be allowed to become too large, in order to avoid the out-of-plane non-focused contribution to the Bragg angle becoming significant. This relatively large out-of-plane range in the detection area may be useful in studying polycrystalline materials.

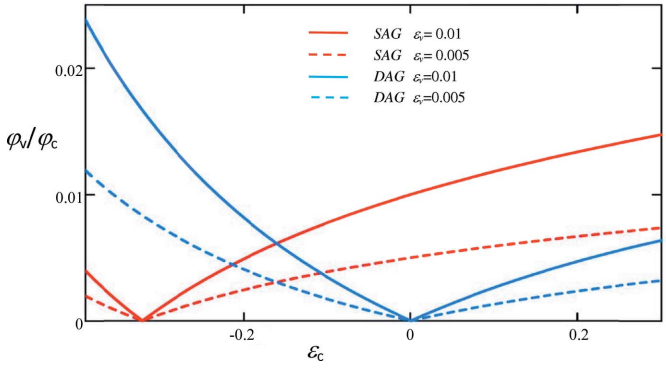

Figure 3
The resolution plotted as a function of ε_c at $\theta_0 = \pi/4$, constant position x', and maxima of $\varepsilon_v = 0.01$ and 0.005 for SAG and DAG, respectively.

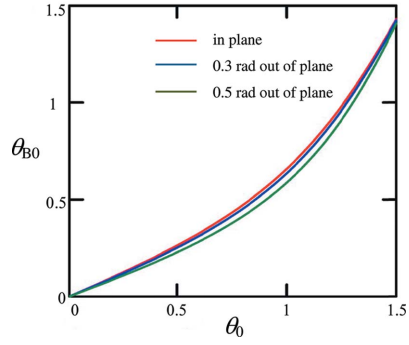

Figure 4
The average Bragg angle $\theta_{B0} = \theta_0 + \varepsilon_{c0}$ where minimal damping is present, plotted as a function of the inclination angle θ_0, in the drawing plane of the figure (red), 0.3 rad out of the plane (blue) and 0.5 rad out of the plane (green).

Fig. 3 shows that the resolution of the SAG at the proper ε_c value is about the same as for the DAG.

Now we will discuss the influence of the uncertainty Δx in the scattering angle x' on the resolution of both the DAG and the SAG.

For the DAG, the resolution remains high over a relatively large angular range x', because $\varphi_{dc}(\varepsilon_c, x', d, B)$ is first-order independent of x'. This is not the case for the SAG, where $\varphi_{sc}(\varepsilon_c, x', d, B)$ changes linearly with x' within the uncertainty Δx, so equations (4) and (5) change to

$$\varphi_{sc}(\varepsilon_c, d, B) = 2cBLd(\cos\varepsilon_c + \sin\varepsilon_c \cot\theta_0), \tag{10}$$

$$\varphi_{sv}(\varepsilon_v, \varepsilon_c, x', d, B) = 2cBLd\left[\varepsilon_v\left(-\sin\varepsilon_c + \cos\varepsilon_c\cot\theta_0 + \frac{2\sin\varepsilon_c}{\sin^2\theta_0}\right) - \frac{x'\sin\varepsilon_c}{\sin^2\theta_0}\right]. \tag{11}$$

The inclusion of the detector uncertainty in $\varphi_{sv}(\varepsilon_v, \varepsilon_c, x', d, B)$, which is not present in the DAG case, equations (8) and (9), is the main advantage of the DAG over the SAG.

For the SAG, at each position $x_0 = 2(\theta_0 + \varepsilon_c)$, the damping of the precession due to a single Bragg reflection can now be written as

$$P(\varepsilon_c, \varepsilon_v, d, B) = A\left[\Delta x, \Delta\varepsilon, \varphi_c(\varepsilon_c, d, B)\right]\cos\varphi_c(\varepsilon_c, d, B), \tag{12}$$

with

$$A\left[\Delta x, \Delta\varepsilon, \varepsilon_c, \varphi_c(\varepsilon_c, d, B)\right] = \left\langle\cos\varphi_v(\varepsilon_c, \varepsilon_v, d, B)\right\rangle_{x', \varepsilon_v} \simeq \exp\left\{-\left[\frac{\alpha(\varepsilon_c, \Delta\varepsilon, \Delta x)\varphi_c(\varepsilon_c, d, B)}{2}\right]^2\right\}, \tag{13}$$

and

$$\alpha(\varepsilon_c, \Delta\varepsilon, \Delta x) \simeq \left\langle\frac{\varphi_v(\varepsilon_c, \varepsilon_v, x', d, B)}{\varphi_c(\varepsilon_c, d, B)}\right\rangle_{x', \varepsilon_v}, \tag{14}$$

where we have assumed a Gaussian distribution for the initial divergence and $\alpha(\varepsilon_c, \varepsilon_v, \Delta x)$ is the half-width of the Gaussian $\exp[-(\varphi_v - \varphi_c/\alpha\varphi_c)^2]$. The maximum resolution expressed by

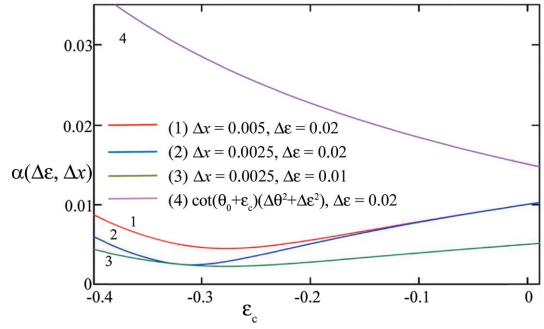

Figure 5
The resolution function $\alpha(\varepsilon_c, \Delta x)$ at $\theta_0 = \pi/4$ as a function of ε_c for two values of Δx and ε_v in three different combinations, labelled (1), (2) and (3). For comparison, the resolution that would be achieved in conventional diffraction for the same angular parameters is shown by the purple line, labelled (4). Here, the incoming divergence was taken as $\Delta\theta = 0.01$.

$\alpha(\varepsilon_c, \Delta\varepsilon, \Delta x)$ is just Δx if $\Delta x < \Delta\varepsilon$. A resolution of $\Delta x = 2 \times 10^{-3}$ may be achievable.

Fig. 5 shows the resolution function $\alpha(\varepsilon_c, \Delta x)$ as a function of ε_c for two different values of Δx and ε_v in three different combinations, together with the resolution expected using conventional diffraction with the same angular parameters. The figure shows that, at the focusing condition $\varepsilon_{c0} = -0.32$, the resolution is fully determined by Δx and, at $\varepsilon_c = 0$, it is fully determined by ε_v. Depending on the value of ε_v, we find a range around ε_{c0} of $-0.33 < \varepsilon_c < -0.25$ where the resolution is more or less constant and only weakly dependent on the initial divergence $\Delta\theta$, which may be much larger [see equations (10)–(14)]. Knowing the instrumental resolution at a certain detector position, the extra damping caused by a diffracting sample as a function of the precession angle directly delivers the Fourier transform of the line shape of that particular reflection.

3. Simulations with SAG

3.1. Polarization for a single crystal

Simulations have been performed in the single-crystal case at different constant angles ε_c around ε_{c0}, with a mosaic spread $\Delta\varepsilon = 0.01$ rad, and with $\Delta x = 10^{-3}$ around $x' = 0$, on a high-resolution position-sensitive detector. Fig. 6(*a*) shows the amplitude of $A(\Delta x, \Delta\varepsilon, \varepsilon_c, \varphi_{sc})$ as a function of the precession angle φ_{sc} at three different ε_c values around ε_{c0}. Fig. 6(*b*) shows the precession at $\varepsilon_c = \varepsilon_{c0}$ at three values of x' over a small phase interval, indicating the shift in phase with changing x'. At $\varepsilon_c = \varepsilon_{c0}$, the precession phase can be followed to about 150 revolutions, and the lattice spacing and changes therein can be determined with an accuracy $\Delta d/d$ of about 10^{-5}. Thus, the phase of the damped precession and changes therein can still be determined with reasonable precision. For that purpose one does not need to measure the whole B range, only one period of the precession angle. With a phase accuracy of 10 mrad the lattice spacing can be determined with a relative accuracy of $\Delta d/d = 10^{-5}$.

3.2. Polarization for polycrystalline samples

In this section we wish to show that the SAG can be used as an inverse-geometry diffractometer. We will use a white beam as the initial beam, with a normalized wavelength spectrum given by

$$I_0(\lambda) = \frac{4}{\pi^{1/2}}\left(\frac{\lambda_T^3}{\lambda^4}\right)\exp\left(\frac{\lambda_T^2}{\lambda^2}\right). \tag{15}$$

Here $\lambda_T = h/(mv_T)$, $v_T = (2kT/m)^{1/2}$, $T = 300$ K, k is the Boltzmann constant, λ is the neutron wavelength and m is the neutron mass. We measure the polarization of the scattered beam at various scattering angles. At each scattering angle, the diffracted intensity of the polycrystal can be considered as coming from a single crystal with a constant average value $\varepsilon_c = (x_0/2) - \theta_0$ and a variable part ε_v with a distribution width given by

$$(\Delta\varepsilon)^2 = \left(\frac{\Delta\theta}{2}\right)^2 + \left(\frac{\Delta x}{2}\right)^2. \tag{16}$$

We use in our simulations a face-centred cubic (f.c.c.) polycrystalline sample as an example, with the following specifications: lattice planes (111), (200), (220), (311), (222) and (400), with a lattice spacing of 0.3 nm.

Because in a polycrystal at each angle x there are lattice planes in reflection, we find for the average polarization by all precession angles $\varphi_{sc}(\varepsilon_c, d, B)$ from equations (10)–(14) using $\varepsilon_c = (x_0/2) - \theta_0$ the average of the N_d weighted contributions from the different lattice planes:

$$P(x_0, B, \Delta x, \Delta\varepsilon) = \Big\{\sum_d N_d I(\lambda_d)\cos\varphi_{sc}\Big(\frac{x_0}{2} - \theta_0, d, B\Big) \times A\Big[\Delta x, \Delta\varepsilon, \frac{x_0}{2} - \theta_0, \varphi_{sc}\Big(\frac{x_0}{2} - \theta_0, d, B\Big)\Big]\Big\} \Big/ \sum_d N_d I(\lambda_d), \tag{17}$$

with

$$A\Big(\Delta x, \Delta\varepsilon, \frac{x_0}{2} - \theta_0, \varphi_{sc}\Big) = \exp\left\{-\left[\frac{\alpha(x_0/2 - \theta_0, \Delta x, \Delta\varepsilon)\varphi_{sc}}{2}\right]^2\right\}. \tag{18}$$

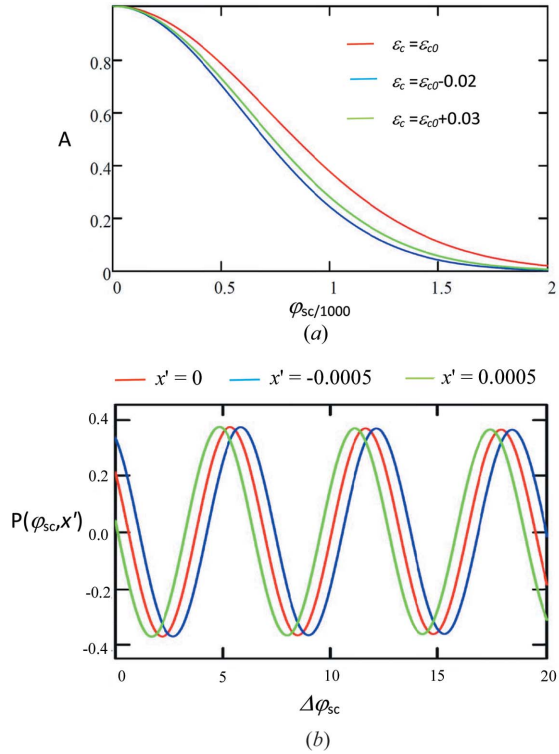

Figure 6
(*a*) The amplitude $A = A(\Delta x, \Delta\varepsilon, \varepsilon_c, \varphi_{sc})$ plotted as a function of the precession phase in the SAG with $\theta_0 = \pi/4$, $\Delta x = 2 \times 10^{-3}$ and $\Delta\varepsilon = 0.01$ for three different ε_c values as indicated in the key. (*b*) The polarization plotted as a function of the precession phase in a small phase interval with $\Delta\varphi_{sc} = \varphi_{sc} - 1000$ rad at $x' = 0$ (red line), $x' = 0.0005$ (green line) and $x' = -0.0005$ (blue line). Here, $\varepsilon_c = \varepsilon_{c0} = -0.32$.

Table 1
Instrumental parameters used in the simulations.

I_{w0}	A_p	b_h	b_w	h_d	L_d	dΩ	Δx	θ_0	$\Delta\theta$	R
10^6 cm^{-2} s^{-1}	0.25	2 cm	2 mm	2 cm	1 m	0.003	0.002	$\pi/4$	0.01	0.1

Here, $\lambda_d = 2d\sin(x_0/2)$ and N_d is the multiplicity factor of plane d in an isotropic distribution in 4π, for which we use $N_{111} = N_{222} = 8$, $N_{220} = 12$, $N_{200} = N_{400} = 6$ and $N_{311} = 24$. Note that the damping as a function of B will be different for each Bragg reflection, meaning that for larger B values the oscillations from the smaller d values are predominantly present. The measured polarized intensity in the detector range Δx is

$$I(x_0, B, t) = V(x_0, t)\left[\frac{1 + P(x_0, B, \Delta x, \Delta\varepsilon)}{2}\right], \qquad (19)$$

with

$$V(x_0, t) = I_{w0}A_p b_h b_w \mathrm{d}\Omega(x_0)\cot\left(\frac{x_0}{2}\right)\Delta\theta R t \sum_d N_d \qquad (20)$$

and

$$\mathrm{d}\Omega(x_0) = \frac{h_d}{L_d \sin x_0}. \qquad (21)$$

Here, $V(x_0, t)$ contains the initial intensity of the white beam I_{w0} with a wavelength spectrum given by equation (15) using $\lambda_T = 0.2$ nm, losses at the polarizers A_p, the beam height b_h, the beam width b_w, the wavelength region $\mathrm{d}\lambda/\lambda = \cot(x_0/2)\Delta\theta$ contributing to each plane reflection, the reflectivity R per plane, the measuring time t per field point B in seconds, and the quantity dΩ determining the fraction of the total scattered neutrons captured by the detector of height h_d and width equal to the beam width at a distance L_d from the sample. In our simulation we took the parameters as given in Table 1. This results in

$$V(x_0, t) = 0.032t\sum_d N_d = 20.4t. \qquad (22)$$

Using these numbers, Fig. 7 shows the simulated intensity as a function of the precession magnetic field B (in mT) at various values of x_0 around $2(\theta_0 + \varepsilon_{c0})$. For the distance L between the inclined precession faces, we used $L = 1$ m. In the intensity $I(x, B, t)$ we included a random number with amplitude $\Delta I = I(x, B, t)^{1/2}$ to account for the expected statistical spread at each point.

From Fig. 7 one sees that, for $B > 20$ mT, the damping becomes considerable for detector angles deviating more than 0.1 rad from the optimal $x = 2(\theta_0 + \varepsilon_{c0}) = 0.93$ rad. The number of visible Larmor precessions is inversely proportional to the observable line width. By Fourier transforming the spectra of Fig. 7, we find the wavelength-dependent intensities shown in Fig. 8.

In the simulation, the instrumental parameters of Table 1 are used with a data-collection time of 10 000 s for 50 similar spectra simultaneously over a total detector angular range of 6°, 50 times the detector width used in the calculations. When the spectra are plotted against $\lambda/\sin(x_0/2)$ and averaged over the whole angular range, the shown spectrum represents the average measured in only 200 s. It has already been shown in §2 that, if a detector height ten times larger is used, the focusing condition in ε_{c0} changes by a maximum of the order of 1% (see Fig. 4), which means that in an optimal detector design the shown spectrum can be obtained in about 20 s measuring time with a resolution much higher than in conventional diffraction.

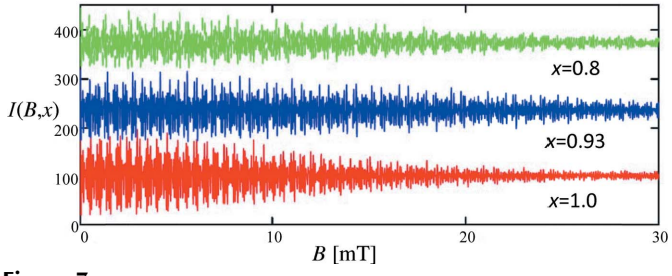

Figure 7
The simulated intensity, in counts per 10 000 s, collected in one detector pixel of $\Delta x = 2$ mrad, plotted as a function of B at various detector angles. 150 has been added to each spectrum to make them more readily distinguishable from each other. Note the different damping of the spectra at the various x values indicated in the figure.

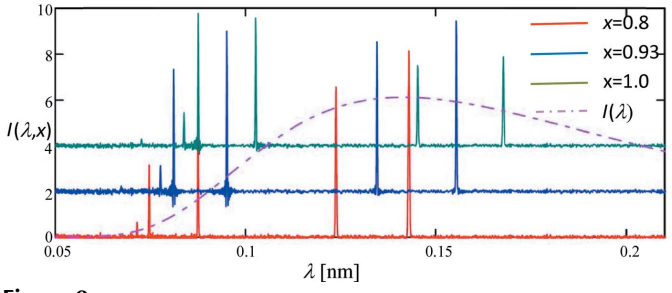

Figure 8
The simulated intensity of an f.c.c. polycrystal plotted as a function of the wavelength λ at three detector positions around the optimal $x = 2(\theta_0 + \varepsilon_{c0}) = 0.93$ rad. The spectra were obtained by Fourier transformation of the simulated intensities of Fig. 7. The dash–dotted line shows the wavelength spectrum used in the simulations.

4. Experiments on single crystals

Experiments have been carried out on an improvised Larmor diffractometer at the reactor institute in Delft, as sketched in Fig. 9. The setup makes use of the resonance technique, where the precession angle is determined by the resonance fields B in

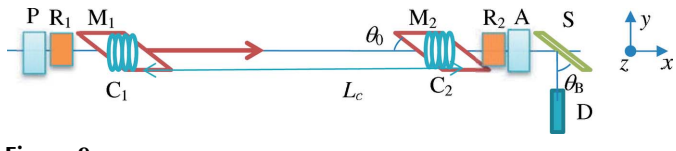

Figure 9
A sketch of the improvised Larmor diffractometer, where P and A are the polarizer and analyser consisting of two polarizing mirror systems, R_1 and R_2 rotate the polarization direction from the initial polarization along z to the xy precession plane and back, M_1 and M_2 are magnets generating the resonance fields B in the resonance coils C_1 and C_2, and S is the sample single crystal to investigate. The precession angle is varied by changing the length L_c by shifting the position of magnet M_1.

two coils a distance L_c apart, similar to what was described by Dalgliesh *et al.* (2011). The precession angle $\varphi_s(\theta, \lambda, B) = 2cBL_c d\cos\theta_B$ is varied in large steps by the resonance field B and in smaller steps by the distance L_c between the magnets by shifting M_1 in the direction of M_2.

Because we could not vary the resonance frequency automatically, we varied the distance L_c only between 80 and 40 cm at various constant fields B and corresponding resonance frequencies to obtain a large enough range of precession angles. At the sample position we placed successively an Si crystal and an Fe_3Si single crystal, at the same scattering angle $\theta = 2\theta_0 = 84^\circ$ and with different mosaic spreads. Fig. 10 shows the results for the Si crystal. The Si crystal consisted of a stack of thin wafers with nearly the same orientation, bent around an axis in the scattering plane to increase the diffracted intensity by deformation. For the damping constant α of the amplitude of the precession defined in equation (13), we found $\alpha(...) = 4.7 \times 10^{-3}$ using an initial polarization of 0.7, shown also in the figure. In the figure the measurements at different fields overlap, which means that in the top part of the figure the measurement at 5 mT is fully hidden by the neighbouring fields.

This $\alpha(...)$ value corresponds to an uncertainty in the wafer orientation of 0.28 mm over the diameter of 50 mm, which is a mosaic spread that may be expected for a stack of separately polished wafers.

Next, we investigated how the amplitude of the precession changes with deviation of the Bragg angle from the inclination angle (Fig. 11). With a fixed open detector over about 10°, we measured the reflected intensity and polarization as a function of the change in Bragg angle, $\Delta\theta_{B0}$. At the minimum and maximum values of $\Delta\theta_{B0}$, where the intensity drops, the polarization amplitude is increased by the effectively smaller angle range contributing to polarization in the detector. In the range where the intensity is roughly constant, the polarization amplitude changes from about 0.1 to 0.05, which corresponds to a change in $\alpha(...)$ of 4.7 to 5.4 $\times 10^{-3}$.

Next, we investigated the reflected intensity and polarization of an Fe_3Si single crystal at the same Bragg angle of 42°. Before measuring the field-dependent polarization, we adjusted the crystal by hand to optimize the detector intensity. Because here we have contributions of different order reflections with different wavelengths, Fig. 12 shows the measured polarization as a function of $f_d = 2cLB\sin\theta_{B0}$, together with the calculated polarization of the three order reflections of Bragg planes (200), (300) and (400) of Fe_3Si in a field of 2.5 mT. The quantity f_d is related to the Larmor phase φ_d of each reflection from the lattice plane d_{hkl} by $\varphi_d = f_d d$. The polarization of the sum of the three orders, $P(f_d)$, fits perfectly with the measured data, with a fitted intensity ratio for the orders I_{200}:I_{300}:I_{400} = 30:15:13, a lattice constant d_{100} = 0.565 nm and polarization amplitude damping according to

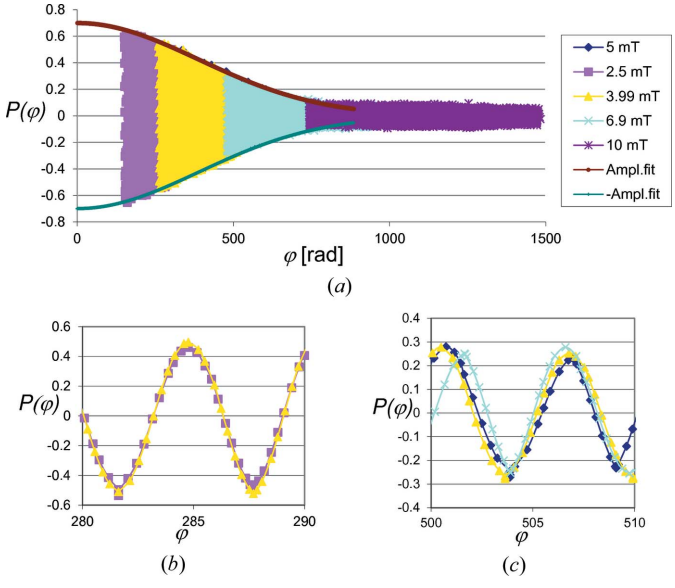

Figure 10
Measured polarization of the reflected beam and amplitude fit on a stack of Si(100) wafers of dimension 50 × 0.3 mm (diameter × thickness). The scattering angle of 84° was twice the inclination angle (42°) of the precession region. The colours and insets refer to the different B fields and resonance frequencies used in the precession region. The lower two figures show $P(\varphi)$ in two small φ ranges at different B values in mT according to the key shown in the inset.

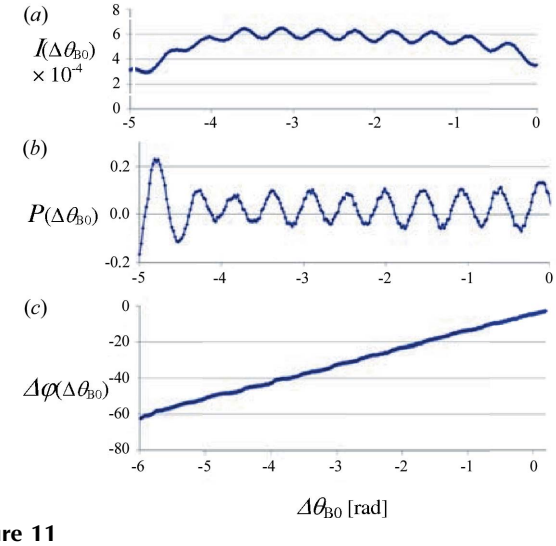

Figure 11
(*a*) Measured intensity as a function of the change in Bragg angle $\Delta\theta_{B0} = \varepsilon$. (*b*) Polarization derived from (*a*) at a fixed field of 5 mT and distance L between the resonance coils of 80 cm, corresponding to a precession angle of 600 rad at $\Delta\theta_{B0} = 0$. (*c*) The change in precession angle derived from (*b*).

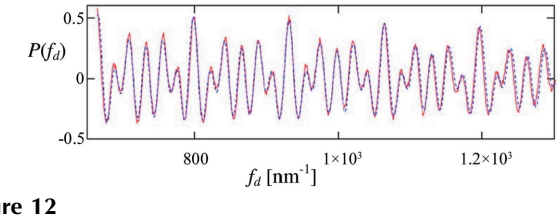

Figure 12
Measured polarization as a function of f_d of the sum of the three order reflections (200), (300) and (400) of an Fe_3Si single crystal (red solid line), together with the calculated polarization (blue dotted line).

$$P(f_d) = \sum_{hkl} \cos(d_{hkl} f_d) \exp\left\{-\left[\frac{\alpha(...) d_{hkl} f_d}{2}\right]^2\right\}. \qquad (23)$$

Here, $\alpha(...)$ is again the uncertainty in the Bragg angle, being the mosaic spread of the crystal. In the fit we have used $\alpha(...) = 4.4 \times 10^{-3}$, close to the damping factor found in the Si diffraction in Fig. 10. For the measurement accuracy of the found lattice spacing, which is only dependent on the phase of the measured polarization, we estimate from this preliminary experiment with three contributing reflections $\Delta d_{100} = 5 \times 10^{-4}$ nm.

5. Discussion

A comparison of the single-arm Larmor diffractometer with the double-arm geometry shows that the DAG is applicable with very little damping at large precession angles and relatively large deviation angles ε_c around $\varepsilon_{c0} = 0$, while the SAG is applicable with somewhat more damping around $\varepsilon_{c0} \neq 0$, albeit with the precession angle linearly dependent on x, making this mode strongly dependent on a high-resolution position-sensitive detector and small angular dimensions of the sample. Note that the resolutions of both modes are, to the first order, independent of the incoming beam divergence $\Delta\theta$. The value of ε_{c0} can be chosen by adjusting the inclination angle θ_0. Both the DAG and the SAG may be candidates for an inverse-geometry diffraction instrument with an initial white beam, with excellent resolution for the DAG and a still high resolution for the SAG, but the latter can have much better counting statistics because it has a much larger angular region x around ε_{c0} and a high angular region perpendicular to the plane determined by the angle x. The latter may be problematic using the DAG because a polarization analyser should also be applied over the large angular region. The large detector solid angle may make the SAG an excellent candidate for an inverse-geometry diffraction instrument with an initial white beam for studying polycrystalline samples, because its resolution and intensity promise to be better than those of conventional diffraction instruments. In comparison with the DAG, the SAG has an advantage for the field arrangement around the precession regions, because it needs only one precession region in front of the sample, and no field arrangements around the sample and detector positions that are fully outside the precession region. As a consequence, the SAG can also be used for magnetic samples without difficult modifications of the setup. The SAG is especially applicable in magnetic and non-magnetic samples. We estimate that sufficient accuracy can be obtained to study relative lattice plane changes larger than 10^{-5}. The SAG is more flexible than the DAG and can be built as a special tool to be implemented in the primary beam of a diffractometer. To compare the DAG and SAG with normal diffraction, both can work with a white beam, thus much higher intensity. Using a large detection angle, in principle all wavelengths of the initial white beam are used in the data collection. Using the latter option, one may concentrate on the variation of different lattice spacings simultaneously by measuring the change in the precession phases of the different lattice spacings in a small field range at high field, thus saving much measuring time in comparison with standard diffraction.

References

Dalgliesh, R. M., Langridge, S., Plomp, J., de Haan, V. O. & van Well, A. A. (2011). *Physica B*, **406**, 2346–2349.

Innosov, D. (2013). *Phys. Rev. B*, **87**, 224425.

Martin, N., Regnault, L.-P. & Klimko, S. (2012). *J. Phys. Conf. Ser.* **340**, 012012.

Niklowitz, P. G., Pfleiderer, C., Keller, T., Vojta, M., Huang, Y. K. & Mydosh, J. A. (2010). *Phys. Rev. Lett.* **104**, 106406.

Pfleiderer, C., Böni, P., Keller, T., Rössler, U. K. & Rosch, A. (2007). *Science*, **316**, 1871–1874.

Rekveldt, M. T., Keller, T. & Golub, R. (2001). *Europhys. Lett.* **54**, 342–346.

Rekveldt, M. T. & Kraan, W. H. (1999). *J. Neutron Res.* **8**, 52–70.

Rekveldt, M. T., Kraan, W. & Keller, T. (2002). *J. Appl. Cryst.* **35**, 28–33.

Repper, J., Keller, T., Hofmann, M., Krempaszky, C., Petry, W. & Werner, E. (2010). *Acta Mater.* **58**, 3459–3467.

Ritz, R., Mühlbauer, S., Pfeiderer, C., Keller, T., White, J., Laver, M., Forgan, E. M., Cubitt, R., Dewhurst, C., Niklowitz, P. G., Prokofiev, A. & Bauer, E. (2010). *J. Phys. Conf. Ser.* **200**, 012165.

Sokolov, D. A., Ritz, R., Pfeiderer, C., Keller, T. & Huxley, A. D. (2011). *J. Phys. Conf. Ser.* **273**, 012085.